

ARTICLE

Open Access

Enhanced multiscale human brain imaging by semi-supervised digital staining and serial sectioning optical coherence tomography

Shiyi Cheng¹, Shuaibin Chang¹, Yunzhe Li², Anna Novoseltseva³, Sunni Lin^{1,3}, Yicun Wu⁴, Jiahui Zhu¹, Ann C. McKee^{5,6,7,8}, Douglas L. Rosene⁹, Hui Wang¹⁰, Irving J. Bigio^{1,3,11}, David A. Boas^{1,3,11} and Lei Tian^{1,3,11}✉

Abstract

A major challenge in neuroscience is visualizing the structure of the human brain at different scales. Traditional histology reveals micro- and meso-scale brain features but suffers from staining variability, tissue damage, and distortion, which impedes accurate 3D reconstructions. The emerging label-free serial sectioning optical coherence tomography (S-OCT) technique offers uniform 3D imaging capability across samples but has poor histological interpretability despite its sensitivity to cortical features. Here, we present a novel 3D imaging framework that combines S-OCT with a deep-learning digital staining (DS) model. This enhanced imaging modality integrates high-throughput 3D imaging, low sample variability and high interpretability, making it suitable for 3D histology studies. We develop a novel semi-supervised learning technique to facilitate DS model training on weakly paired images for translating S-OCT to Gallyas silver staining. We demonstrate DS on various human cerebral cortex samples, achieving consistent staining quality and enhancing contrast across cortical layer boundaries. Additionally, we show that DS preserves geometry in 3D on cubic-centimeter tissue blocks, allowing for visualization of meso-scale vessel networks in the white matter. We believe that our technique has the potential for high-throughput, multiscale imaging of brain tissues and may facilitate studies of brain structures.

Introduction

The human brain consists of an estimated 86 billion neurons¹, which form intricate connections and networks that underlie the complex functions. To gain new insights into the brain, major efforts have recently been made to develop multiscale imaging technologies for visualizing anatomical structures with microscopic resolution across cubic centimeters of tissue. The most widely used techniques for visualizing anatomical and neuronal structures are based on histological staining. Gallyas silver staining is used to characterize myelin content and neuronal structures, as well as to identify pathological features of

neurodegenerative diseases in human brain tissue^{2,3}. To create a high-resolution 3D model of the cytoarchitecture, the BigBrain project⁴ reconstructed a whole human brain with more than 7000 histological sections, which involves slicing the tissue into 20- μ m sections, staining with silver halide to reveal cellular and fiber structures, and registering the slices in 3D. However, these histological staining processes are generally complex, labor-intensive, time-consuming, and prone to experimental error and staining variability. Furthermore, the slicing, mounting, dehydration, and staining inevitably cause tissue damage and slice-specific distortions, which can limit the accuracy of 3D alignment and reconstruction of structures at the micron scale^{5,6}. Therefore, there is a growing need for developing 3D pathology imaging techniques, especially label-free techniques that can provide high-resolution 3D visualizations of brain tissues with minimal tissue damage

Correspondence: Lei Tian (leitian@bu.edu)

¹Department of Electrical and Computer Engineering, Boston University, Boston, MA 02215, USA

²Department of Electrical Engineering and Computer Sciences, University of California, Berkeley, CA 94720, USA

Full list of author information is available at the end of the article

These authors contributed equally: Shiyi Cheng, Shuaibin Chang, Yunzhe Li

© The Author(s) 2025



Open Access This article is licensed under a Creative Commons Attribution 4.0 International License, which permits use, sharing, adaptation, distribution and reproduction in any medium or format, as long as you give appropriate credit to the original author(s) and the source, provide a link to the Creative Commons licence, and indicate if changes were made. The images or other third party material in this article are included in the article's Creative Commons licence, unless indicated otherwise in a credit line to the material. If material is not included in the article's Creative Commons licence and your intended use is not permitted by statutory regulation or exceeds the permitted use, you will need to obtain permission directly from the copyright holder. To view a copy of this licence, visit <http://creativecommons.org/licenses/by/4.0/>.

and distortion, and that can reduce the need for physical staining (PS)^{7–10}.

Optical coherence tomography (OCT) is a label-free imaging technique that allows high-resolution 3D visualization and quantification of intrinsic optical properties of tissue, such as the scattering coefficient and back-scattering coefficient^{11,12}. Recently, OCT has shown great promise in brain imaging applications, such as visualizing single neurons¹³, fiber tracts¹⁴, and the laminar structure of the cerebral cortex in the human brain^{15,16}. While traditionally limited by light penetration, serial sectioning OCT (S-OCT) integrates OCT with a vibratome slicer to enable 3D imaging of cubic centimeters of tissue¹⁷. S-OCT permits straightforward and accurate 3D high-resolution reconstruction of large-scale brain anatomy, microstructures, and tractography^{17–19} with minimal tissue distortion. This is achieved through the use of a serial imaging protocol²⁰, where OCT imaging of the top ~150 μm thick tissue is alternated with the slicing off of the superficial tissue, thus reducing cutting-induced distortion after imaging. This enables accurate reconstruction of the complex 3D structures of brain tissues without requiring sophisticated inter-slice registration algorithms. Despite its ability to routinely generate large-scale volumetric brain imaging data, S-OCT still requires considerable expertise to identify and annotate anatomical and neuronal features for further analysis^{11,14,17,21}. Our goal is to augment S-OCT with a digital staining (DS) technique that enables 3D histology on large-scale human brain tissues.

In recent years, deep learning methods have revolutionized the field of DS, which aims to transform label-free images into histological staining-like images using computational models^{22,23}. DS offers a fast and low-cost alternative to conventional PS methods. Several DS models have been developed to perform transformations between various input-output imaging modality pairs. Most existing DS methods are based on supervised learning, necessitating paired images of tissue slices with and without staining for model training. To ensure accurate DS results, pixel-level cross-modal registration between the image pairs is crucial^{24–27}. However, acquiring such paired images is challenging and often involves sophisticated image registration procedures^{22,25}. To overcome these challenges, recent studies have explored unsupervised image translation models for DS, which only need unpaired collections of images from the two modalities for training^{8,23,28–31}. The most widely used unsupervised method is CycleGAN³², which employs two sets of generators and discriminators to enforce cycle consistency and content preservation in the image translation task. Another method, Contrastive Unpaired Translation (CUT)³³, uses contrastive learning to maintain structural and content preservation with only one set

of generator and discriminator, demonstrating improved training efficiency in DS tasks²⁹. Despite these advancements, unsupervised models generally still lag behind their supervised counterparts in terms of accuracy²². Recent work has also explored formulating loss regularizations by incorporating properties of misaligned medical images. Reg-GAN introduced loss-correction theory to integrate unsupervised registration into the training process, showing improvements in simulated single-modality data³⁴. Additionally, DS methods have been found useful in enhancing multi-modal deformable registration performance^{35,36}. However, these unsupervised methods, while leveraging geometric similarities, often overlook essential content mismatches in realistic multi-modal data, making them susceptible to generating artifacts or hallucinations.

In this study, we introduce a novel *semi-supervised* learning model specifically designed for DS using *limited* and *weakly paired* image data, addressing the complex challenge of aligning essentially unpairable multi-modal imaging modalities. We define this challenge as “weakly paired DS” and propose a robust training framework featuring two novel semi-supervision augmentation modules aimed at mitigating hallucination effects inherent in the unsupervised backbone network. To rigorously evaluate our approach, we have developed a novel evaluation pipeline that allows for the application of widely used metrics for paired images to our weakly paired images. To demonstrate the practical utility of our model, we apply it to translate S-OCT images into Gallyas silver staining, with the goal of enhancing volumetric human brain imaging. This application not only showcases our model’s ability to reduce staining variability but also its effectiveness in preserving the 3D geometry of large-scale human brain tissue blocks. Furthermore, we have conducted extensive quantitative analyses using pathology-feature-based metrics to underscore the advantages of our DS model over traditional physical staining methods, highlighting its potential for 3D histology applications.

Our model backbone is based on the unsupervised CUT framework, enabling DS using unpaired training data. This module combines contrastive learning and adversarial learning to address the lack of paired imaging data, as the physically stained images were obtained from unordered adjacent brain tissue sections to the OCT-imaged sections, and were confounded by tissue damage and distortion during the staining process. To improve the accuracy of the unsupervised model, we introduce semi-supervision through two auxiliary tasks. First, we devise a pseudo-supervised learning module that trains the DS network on a pseudo-paired training dataset generated using our previously established biophysical model. Our prior work has revealed a statistically significant linear correlation between the OCT scattering

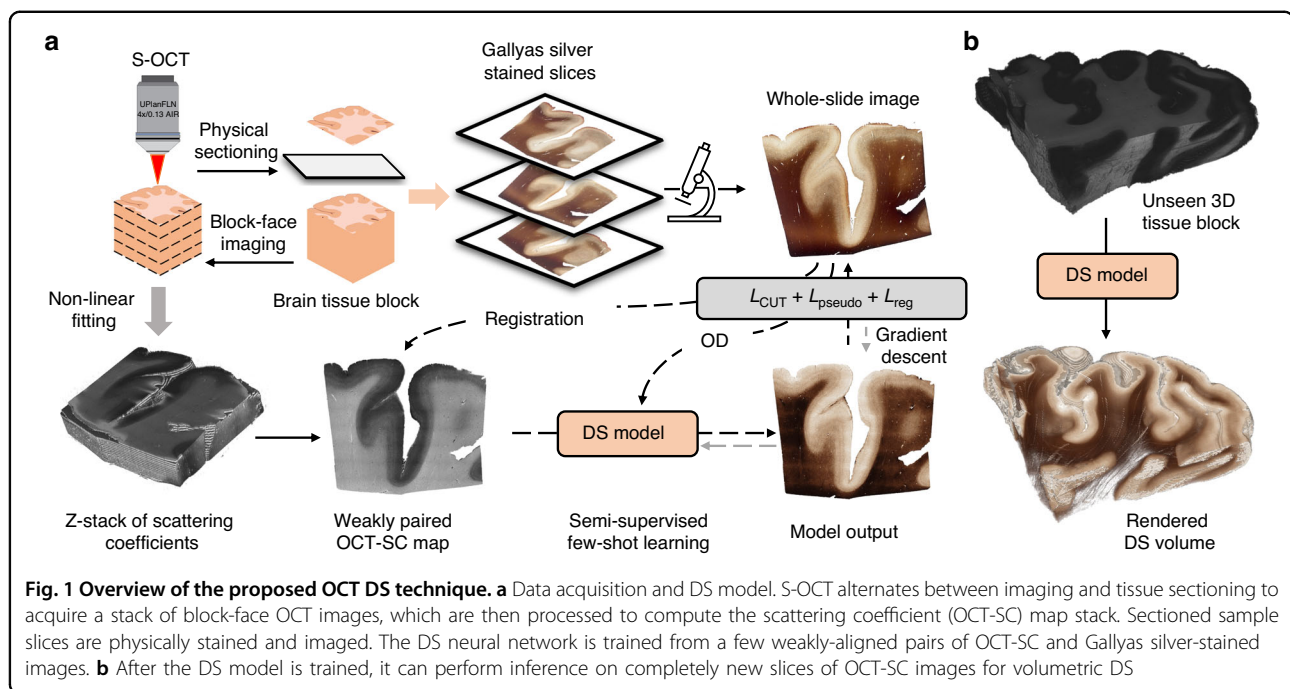
coefficients (SC) and the optical density (OD) derived from the Gallyas silver stained images²¹. However, this relationship, while indicative of a general trend, is subject to considerable variability across individual samples due to biological differences and other factors. Leveraging this similarity prior, our pseudo-supervised learning module learns to translate the generated OD back to the Gallyas silver stain, serving as a proxy for supervising the translation from OCT-SC to Gallyas silver stain. This naturally pixel-aligned pseudo-supervision effectively augments the training data, enabling the DS model to be trained despite the limited availability of human brain samples. Moreover, when combined with the adversarial learning component in the CUT backbone, the domain gap between the OCT-SC images and OD maps is effectively mitigated by domain-adversarial training³⁷. Second, we develop an unsupervised cross-modality image registration module that aligns the adjacent Gallyas image with the OCT-SC image. This module enables the DS model to utilize the geometric similarity information provided by adjacent slices, thereby guiding the image translation process. To train the registration network effectively, we introduce a novel two-stage, multiscale training strategy. This strategy enables the network to learn image registration at the “global” whole slide image (WSI) scale while simultaneously learning image translation at the “local” image patch scale. Furthermore, this collaborative training approach between the DS model and the registration model results in more effective enforcement of high-quality DS results.

We present our DS pipeline for data acquisition and deep learning model training in Fig. 1a. We use S-OCT to obtain label-free volumetric data of human brain samples. We then process the OCT data to calculate the SC maps¹¹ (see details in Methods). Next, we develop a deep learning DS model that transforms OCT-SC images into Gallyas silver stain images. We choose OCT-SC as the input for the DS model instead of the raw OCT measurements because SC measures the intrinsic optical properties of the tissue and eliminates the inhomogeneity in the raw OCT intensity by using a nonlinear model-fitting process¹¹. Moreover, a biophysical model from our previous work showed that OCT-SC mainly depends on the contribution of myelin content, which is captured by the OD of the Gallyas silver staining²¹. We hypothesize that the statistical correlation between these two modalities can be leveraged to create a more accurate image-to-image mapping using a deep learning model. During S-OCT, we also collect a few unordered tissue slices that are physically stained for DS model training and evaluation. The deep learning model is trained on a few weakly-aligned pairs of OCT-SC and Gallyas silver stained WSIs. The inference stage of the DS model is shown in Fig. 1b. After the model is trained, it can be applied on any OCT-

SC maps to enable 3D neurohistology on cubic centimeters of brain tissue and visualize mesoscopic brain structures.

First, we present the OCT DS results on single-section tissues from various cerebral cortex samples and compare them with PS results from adjacent sections. We demonstrate that DS exploits the quantitative nature of OCT-SC and thus can produce consistent staining quality across different samples. Compared to PS, DS reveals comparable mesoscopic ($\sim 10\ \mu\text{m}$) structures in different tissue regions without introducing staining variability across samples and experiments. In addition, we show that DS enhances contrast across cortical layer boundaries and can consistently differentiate cortical layers IV, V and VI. Next, we show a 3D-rendered volumetric DS result on a cubic centimeter-scale tissue block that was not used for training the DS model. The result shows geometry-preserving 3D staining on large-scale brain tissue and visualization of vessel structure in the white matter region. Finally, we showcase a pilot study on the generalization performance of our method - we apply the DS model trained on cortex regions to samples from other anatomical regions acquired from different OCT setups.

In summary, we present a novel deep learning technique for DS of OCT images for large-scale human brain imaging. Our method allows direct visualization of important mesoscopic 3D brain features, including myeloarchitecture of the cerebral cortex and main 3D blood vessel network in the white matter, with contrast that closely resembles Gallyas-silver staining. Our method has several advantages over traditional PS, including reducing staining variability, preserving complex brain 3D geometry, and facilitating volume generation across cubic centimeters of tissue. Additionally, our method enhances the interpretability of the label-free OCT modality for brain imaging. This unique combination, as highlighted in Fig. S1, makes our method appealing to high-throughput 3D neuropathology applications. However, our method faces some limitations originating from our current S-OCT system, such as artifacts from image stitching^{12,14}, uneven tissue sectioning, speckle noise, and limited lateral and axial resolution due to the SC model fitting. Although our technique is sensitive to fiber structures in the gray matter, the speckle noise and limited resolution resulted in discontinuities and grainy artifacts in the DS results. We expect that these issues will likely be overcome by future generations of high-resolution S-OCT systems^{38,39} and improved processing algorithms. Despite these current limitations, we believe that our semi-supervised learning-based DS framework holds broad applicability for other bioimaging modalities and DS applications. Furthermore, our work has significant implications for quantitative volumetric neuropathology. The integration of DS techniques with S-OCT has great potential for high-



throughput, multiscale human brain imaging. The data generated from this technique could help better understand the meso- and micro-structure of brain tissues and their role in disease development, and ultimately enhance our knowledge of the brain structure and function.

Results

Digital staining by semi-supervised learning using weakly-paired images

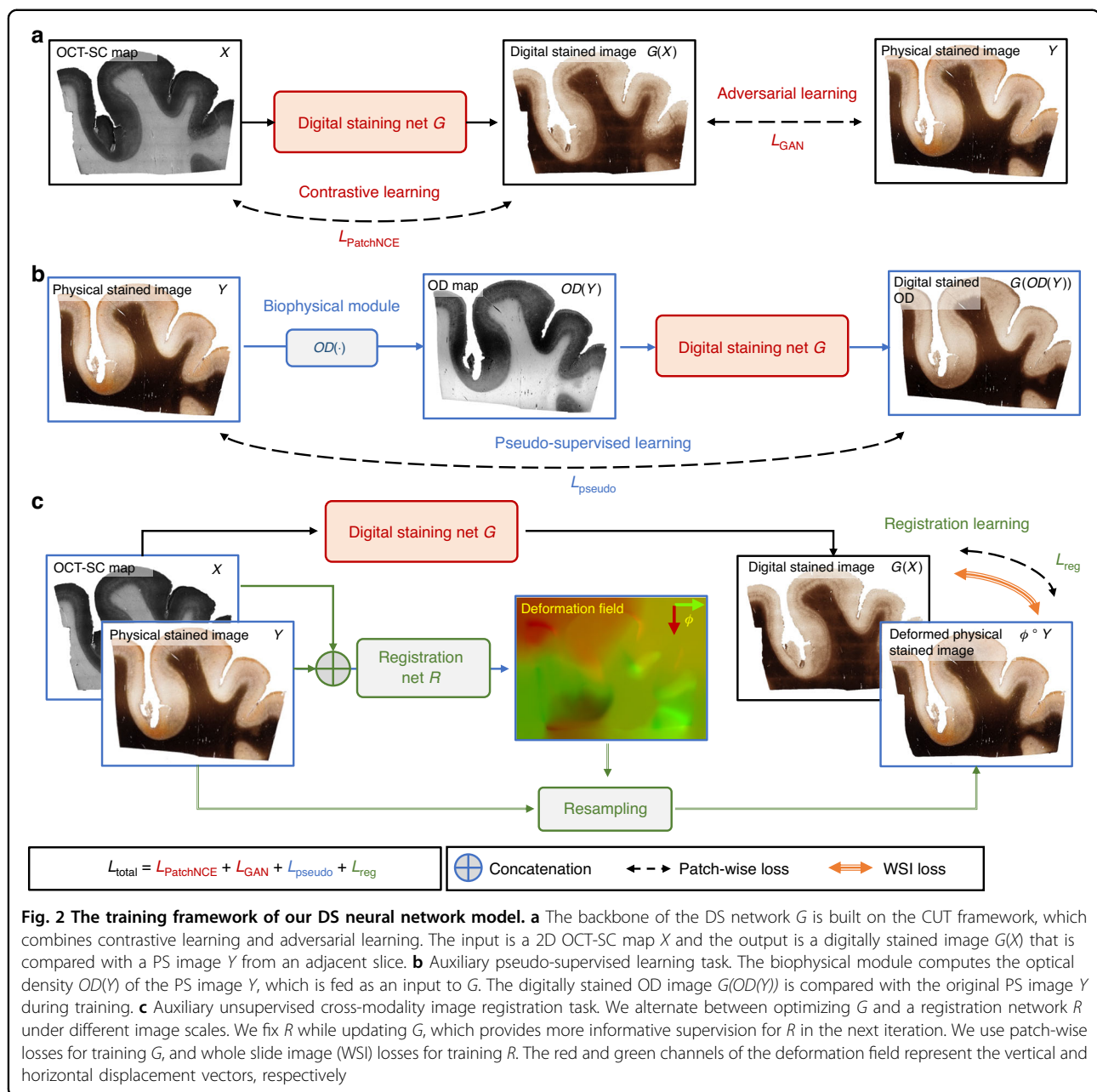
We formulate the DS task as a weakly-paired image translation problem because we do not have access to pixel-aligned image pairs of OCT-SC and PS images. To achieve better performance than fully unsupervised methods, we exploit the side information provided by the structural and content similarity between the adjacent sections in the imaging data, as well as a biophysical model for linking OCT-SC and the contrast in Gallyas silver stain in a semi-supervised deep learning framework.

The training framework of our DS network consists of several novel learning components, as shown in Fig. 2. Based on the CUT framework as the backbone³³, the DS model uses a mix of adversarial loss and contrastive loss in the unpaired image setting, as shown in Fig. 2a. The adversarial learning measures the perceptual similarity of the generated DS images and the PS images. It tries to reduce the gap between the high-dimensional distributions of the DS and PS images such that the generated DS images are perceptually indistinguishable from the PS images. The contrastive loss uses self-supervised patch-wise learning to ensure structural consistency between the OCT-SC and DS images. It maximizes mutual information and provides self-guidance for

content preservation. The combination of contrastive loss and adversarial loss enables high-quality DS images that preserve the content and structures of the OCT-SC images.

To improve upon the unsupervised CUT framework, we propose a semi-supervised learning method. Our method leverages augmented pseudo pairs generated by a biophysical model and registered cross-modality image pairs that are dynamically adjusted by a learnable registration network. The intuition is that using additional auxiliary supervision enhances the learnability, efficiency and accuracy of the model compared to unsupervised learning. Crucially, our semi-supervised method does not require any exact paired PS and OCT-SC images during training.

In Fig. 2b, we introduce the pseudo-supervised learning auxiliary task to enhance the unpaired image translation for DS of OCT-SC images. We first compute the OD maps from the PS images and then utilize the OD - PS image pairs to train the DS model in a pseudo-supervised manner. This approach proves effective because the OD image exhibits similar image contrast and feature distribution as the OCT-SC across various cortical regions. Additionally, the OCT-SC demonstrates an approximate linear relationship with the OD of the Gallyas silver stain²¹. Furthermore, since the OD map is naturally pixel-aligned with the PS image, it facilitates supervised learning and provides additional semi-supervision and alignment constraints for the main DS model. However, the inherent disparities in image features and intensity value distributions between the OD map and the OCT-SC image result in a domain gap, which limits the accuracy of



the trained DS model when relying solely on this auxiliary task. Our insight is that when this task is combined with the adversarial learning component in the CUT backbone, it enables domain adaptation similar to the domain-adversarial training framework³⁷. The performance on the OCT-SC image is ensured by penalizing the perceptual differences between the DS images generated from the OCT-SC image and the OD map using the adversarial loss. By leveraging both the pseudo-supervised learning and adversarial learning components, we effectively bridge the domain gap and improve the accuracy of the DS model for OCT-SC image translation.

In Fig. 2c, we illustrate the second auxiliary task for aligning the PS image, the OCT-SC image, and the DS image using a registration network. This registration module undergoes two training stages: pre-training and fine-tuning. During the pre-training stage, the registration module operates on the WSI scale. It predicts a deformation field that indicates the pixel-wise displacement vectors required for non-rigid transformation. To facilitate cross-modal self-supervised registration, we utilize the OD map as a surrogate for the OCT-SC image and learn a deformation field between the OD map and the input OCT-SC image. This result is used as an initial

estimate for the deformation between the PS image and the matching OCT-SC image. By leveraging our biophysical model, we bootstrap the challenging self-supervised cross-modality image registration problem in this pre-training stage. The subsequent fine-tuning of the registration model aims to provide pixel-wise weak-supervision for the DS model. In this stage, we employ an alternate training approach that involves collaborative learning between the DS model and the registration model. When the DS model is fixed, the registration model is trained at the WSI scale to address global geometry correction. When the registration model is fixed, the DS model is trained at the image patch scale to provide sufficient samples for local translation learning. This unsupervised cross-modality image registration module enables the DS model to learn improved local color tone mapping from unaligned imaging modalities without the need for explicit supervision.

Overall, our DS framework enhances unpaired image translation through pseudo supervised learning and unsupervised cross-modality image registration. The total loss function used for training is the weighted sum of the four objectives derived from the main image translation task and two auxiliary tasks. Our method demonstrates superior performance compared to baseline methods, including CycleGAN, CUT and FastCUT, in terms of DS quality and accuracy, as detailed in Supplementary Sections 2 and 3, and illustrated in Figs. S2, S4, and S5.

Detailed information on the network structure, training procedures, and quantitative evaluations is provided in the Methods section and Supplementary Sections 4, 5, 10, and 11. Beyond improvements in quantitative metrics, our new model training strategy offers several advantages over previous unsupervised approaches. We compare and analyze these advantages in Supplementary Table S1. Additionally, we perform a quantitative evaluation of network hallucination using a customized fidelity score, as shown in Supplementary Fig. S5.

Furthermore, we present several ablation study results to justify the inclusion of each training component in our DS model, as detailed in Supplementary Section 12 and Fig. S13. These comprehensive evaluations underscore the robustness and effectiveness of our proposed framework in achieving high-quality DS for unpaired image translation.

Digital staining enhances mesoscopic brain structures and provides high staining uniformity

We present the ability of our DS technique to preserve the mesoscopic brain structures and achieve uniform staining of cerebral cortex sections from post-mortem human brains. We use two groups of PS imaging results as comparative references: one group consists of WSIs of

well-stained sections, and the other group consists of WSIs of less-ideally-stained sections.

In Fig. 3a, we present the OCT-SC, DS, and well-stained PS images of adjacent sections from the human cerebral cortex, arranged from left to right. The DS images show that our technique can accurately capture various brain structures that match the PS images, such as cortical layers, myelin fibers, and vessel blobs. Here myelin fibers refer to myelinated axon bundles that consist of multiple axons, which can be resolved with 12 μm resolution in our S-OCT system. This is validated in Supplementary Fig. S15. The DS and PS images share similar contrast, with white matter regions appearing as dark brown or black and gray matter regions appearing as white, while the OCT-SC image has the opposite contrast. Within the gray matter, the infra layers also appear to be darker than supra layers, consistent with the PS images. These correspondence in mesoscale structures validate that our DS model can reliably and accurately learn this general inverse mapping between OCT-SC and PS images.

In the zoom-in regions, we present the images on different types of cortex regions, including gyral crest regions marked as 1 and 3 and sulcal fundus regions marked as 2 and 4, from the three modalities: OCT-SC, DS and PS. In region 1, the structures of radial myelin fiber bundles at scales of about 10–20 μm are shown as dark brown tubular features in both DS and PS images, especially in the gray matter region. By comparing OCT-SC and DS images, we can see that the image content is consistent, which indicates that the ability of resolving fine features is primarily limited by the input OCT-SC data. Despite the limitations of resolution and speckle noise in the OCT data, the orientation of fiber bundle traces and the intensity distribution according to cortical layers can still be discerned in the DS results. Similar patterns are also evident in zoom-in regions 3 and 4, where the local intensity variation is visible in the gray matter regions, although the fiber bundles are less distinct in OCT-SC and DS images than in the PS images. In region 2, the supra cortical layers (I–III), infra layers (IV, V, VI) and white matter are clearly distinguished by the white, light brown, and dark brown bands, respectively. The black line structure near the top of the PS image indicates smaller vessels, which are also visible in the DS image at the same locations. The zoom-in regions 1, 2, and 3 in PS show small white blob or tubeness features especially in the white matter regions. In PS, these white blobs represent the empty space previously occupied by vessels which are lost due to slicing and washing steps during staining. In contrast, the white blobs in DS images primarily represent the space within vascular walls and perivascular space which appear smaller since no thin slicing or physical staining is performed on OCT-SC images. Those features are generally referred to as VS

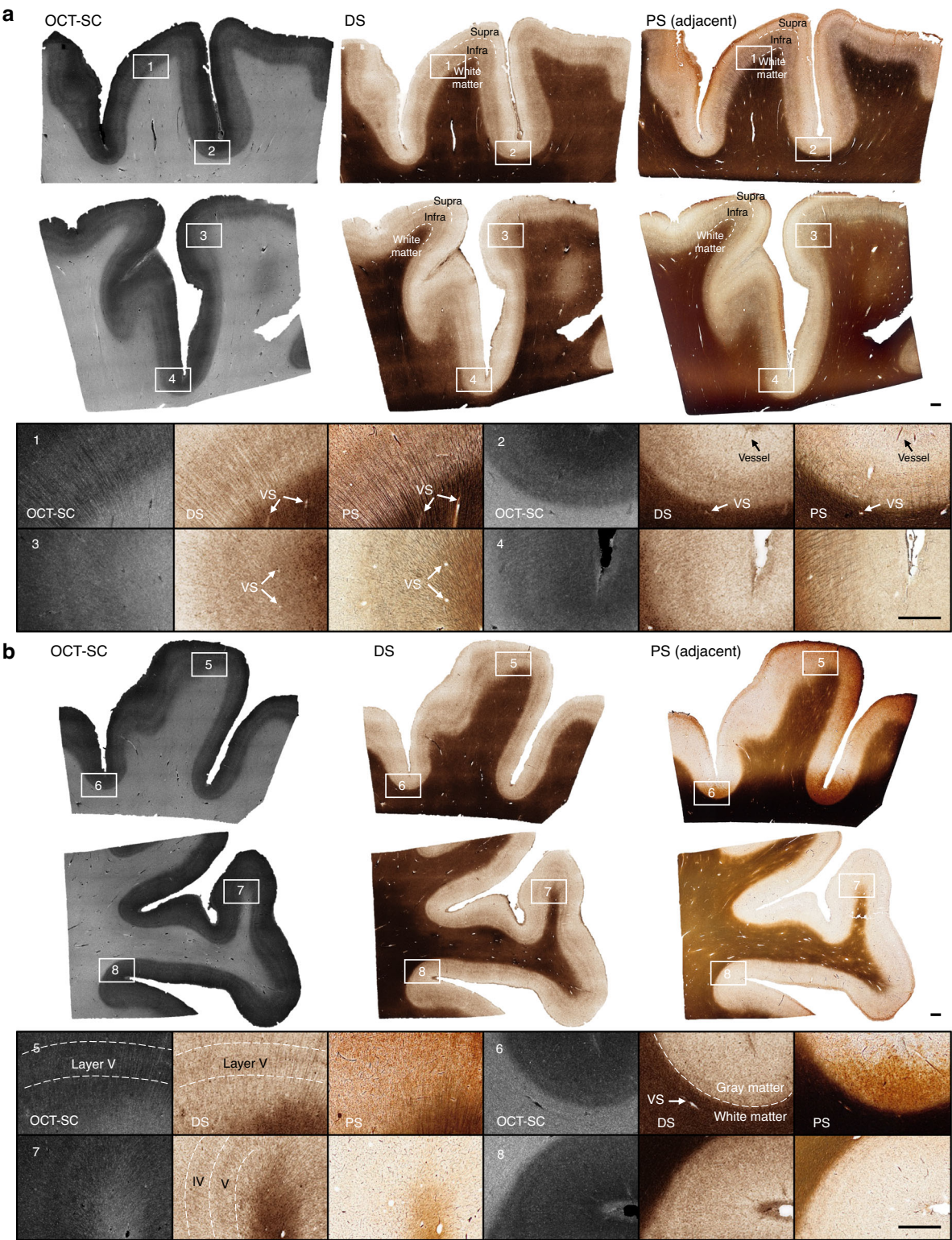


Fig. 3 DS results on OCT-SC of tissue slices and comparisons with PS images. Cases include **(a)** ideally stained slices; **(b)** non-uniformly stained and under-stained slices. ROI 1, 3, 5, and 7 are gyral crest regions and 2, 4, 6, and 8 are sulcal fundus regions. VS: “vessel space”. Scale bars are 1 mm. The second slice in **(a)** is an independent testing slice from a subject that also contributed other slices in the training set, while all other shown slices are from entirely independent testing subjects

(“vessel space”) in Fig. 3. These visualizations demonstrate that our DS model can faithfully preserve $\sim 20\ \mu\text{m}$ scale brain structures captured by S-OCT^{17,19,38}.

A major advantage of DS over PS is stain uniformity. To demonstrate this, we present three types of images in Fig. 3b from the less-ideal PS group that comprises most of our PS data. One inherent limitation of traditional histological staining is the variability across different sample regions and experiments. Despite our careful sample preparation and staining procedures, the staining result is influenced by many confounding factors of the chemical reaction, and uniformity of the staining quality is challenging to ensure. In Fig. 3b, the rightmost column of the first row shows a PS example with over- and non-uniform staining (in particular along the vertical directions); the second row shows a PS example with under-staining.

We select two gyral crest regions (marked as 5 and 7) and two sulcal fundus regions (marked as 6 and 8) to provide in-depth analysis. The PS images in regions 5 and 6 are over-stained, while the PS images in regions 7 and 8 are under-stained. In region 5, the DS and OCT-SC images show clear ridges corresponding to cortical layer V, but the PS image shows a dark brown shade due to over-staining. In region 6, which is a sulcal fundus region with less visible cortical layers, the DS image shows a clear boundary between white matter and gray matter regions, but the PS image shows an ambiguous boundary. Small vessel blobs are also more visible in the DS image than in the PS image. In region 7, which is a gyral crest region, the DS image shows dark ridge features corresponding to cortical layer IV and V, but the PS image does not show these features due to under-staining. Additional examples are shown in Supplementary Section 6 and Fig. S6.

The superior stain uniformity demonstrated by our DS results across different sections is facilitated by the OCT-SC, which extracts a normalized quantity based on a physics model reflecting the intrinsic properties of brain tissue. This uniformity offers significant advantages for anatomical and pathological evaluations. To highlight the improved staining uniformity compared to traditional physical staining methods, we performed a detailed quantitative analysis, as described in Supplementary Section 16 and illustrated in Fig. S18. A limitation of our current OCT-SC curve fitting model is that it reduces the spatial resolution (lateral: $6\ \mu\text{m}$ raw OCT measurement, $12\ \mu\text{m}$ fitted SC map; axial: $6\ \mu\text{m}$ raw OCT measurement, $150\ \mu\text{m}$ fitted SC map), which limits the ability to resolve fine fiber structures.

Digital staining enables reliable cortical layer differentiation and layer thickness quantification

We demonstrate the capability of DS-OCT to reliably distinguish cortical layers with comparable or even better

sensitivity than PS, thanks to the uniform DS quality as discussed before. We identify cortical layers IV, V, and VI by the displayed fiber density^{40,41}, since these layers are more prominent than layers I, II, and III in most of our samples. We provide additional examples of DS layer visualization and compare them with well-stained and less-ideal stained PS samples in Supplementary Section 7 and Fig. S7. We also show how the layer thickness can be consistently quantified in our DS images.

Figure 4a shows the WSIs of the DS result and the reference PS of an adjacent brain slice. The DS image clearly reveals the curved double-band structures above the white matter region, which are stained in dark brown. These features indicate higher myelin fiber density that are characteristic in cortical layer IV and V⁴¹. Consistent image contrast variations for the laminar structures are observed in the DS result. In contrast, the double-band structures are less visible around some of the gyral regions, and the contrast is less distinct in the PS image. Figure 4b shows zoom-ins from a gyral crest region and a sulcus region of the three modalities, corresponding to the regions marked by the green box and red box in Fig. 4a, respectively. The OCT-SC and DS images have a strong correlation in their intensity variations. The DS image consistently shows the double-band features in the gray matter region, while the PS image often fails to reveal them due to over- or under-staining.

Next, we demonstrate the improved contrast between cortical layers in DS by plotting the average intensity (across the three color-channels) along the white dotted lines in Fig. 4b. The right panel shows the normalized profiles over a 3.5-mm depth range, where blue, green and red represent OCT-SC, DS and PS modalities, respectively. We manually marked the boundaries of layer IV, V, and VI with dotted vertical lines in four different colors. In both gyrus and sulcus regions, the DS profiles show the highest contrast (measured by the difference between the maximum and minimum values) in layer IV and V among the three modalities, which facilitates identifying the layer boundaries. When comparing OCT-SC and PS with DS, the DS enhances the intensity variations at the boundary between layer IV and V. This reduces any confusion when distinguishing between these two layers. Comparing the profiles between OCT-SC and DS in different layers suggests that our DS model works beyond our approximate linear biophysical model²¹ and increases the local contrast by a nonlinear mapping function expressed by our neural network. This argument is further supported by a color-intensity correlation analysis detailed in Supplementary Section 14 and Fig. S16.

In Fig. 4c, we further demonstrate straightforward segmentation and thickness quantification of cortical layers IV, V, and VI using our DS result (see details in Methods), which can provide valuable information for many

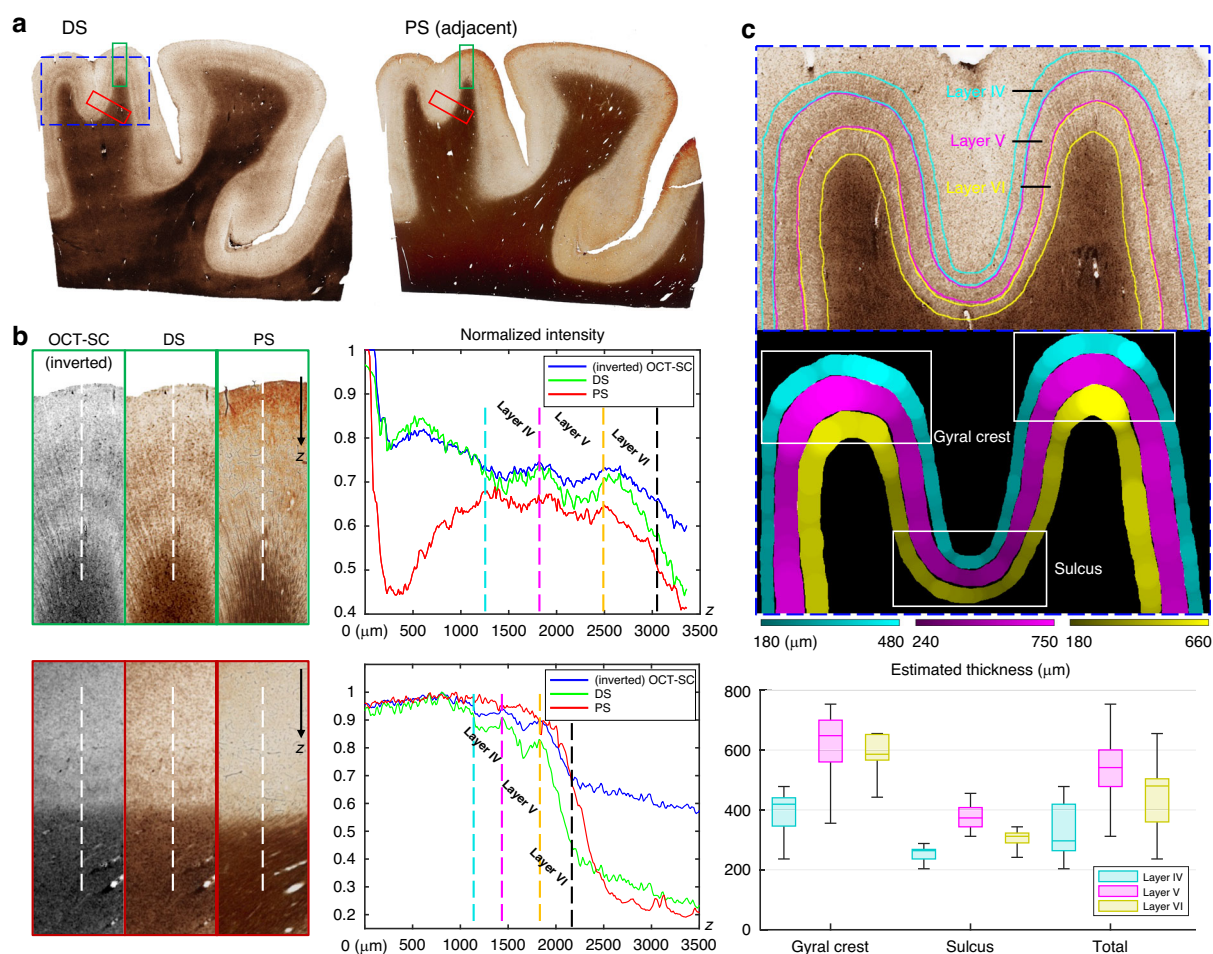


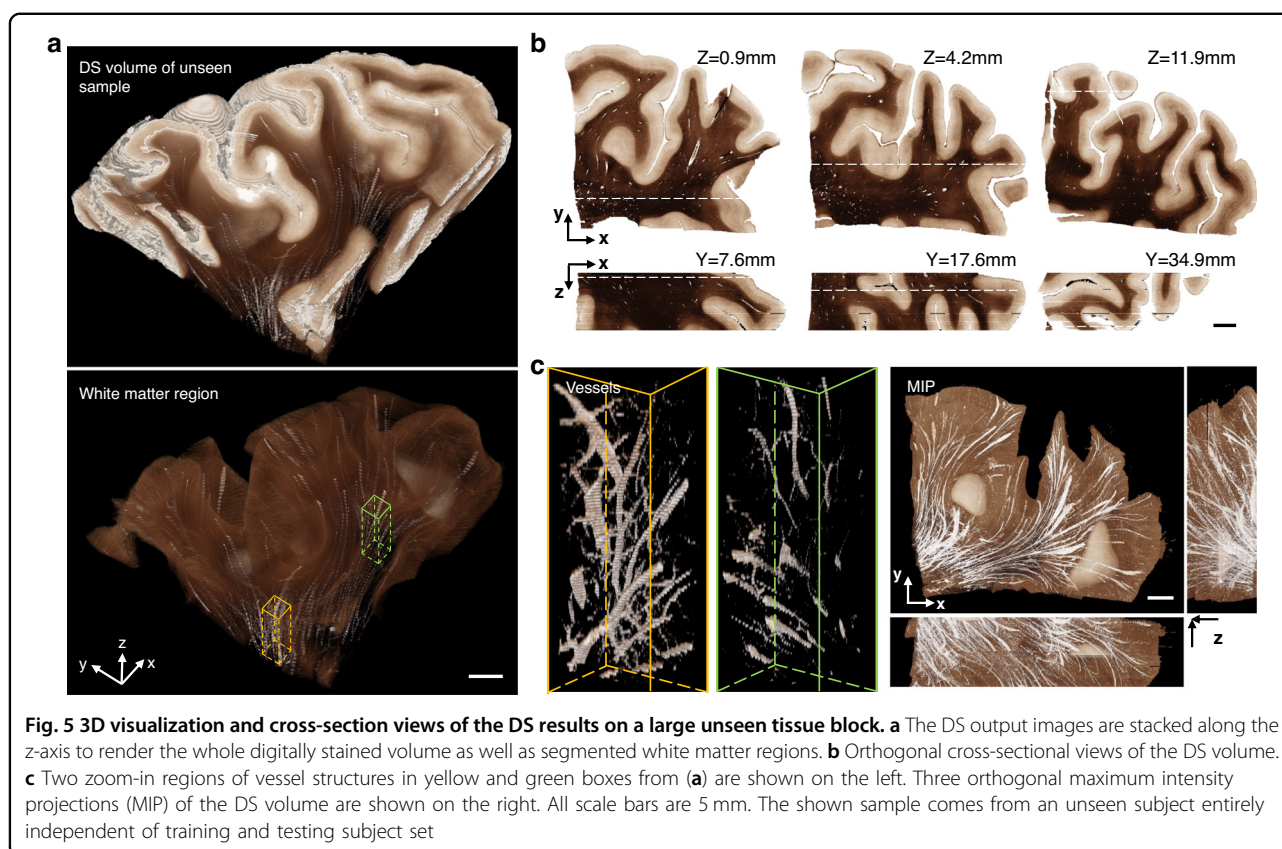
Fig. 4 Comparisons results of layer differentiation and thickness estimation in DS results. **a** The DS and PS WSIs from a cortex tissue section. **b** Zoom-in ROIs of inverted OCT-SC, DS and PS modalities marked in green and red boxes in **(a)** and normalized intensity profiles aggregates along white dotted lines. **c** Manually annotated layers IV/V/VI labeled in three colors and estimated local thickness. Statistics of thickness are visualized in box plot and grouped by gyral crest and sulcus regions. ROI is the zoom-in of the dotted blue box from **(a)**. The shown slice is an independent testing slice from a subject that also contributed other slices in the training set

neuropathological studies^{17,42,43}. The top panel shows the zoom-in region of the dotted blue box in Fig. 4a, where we manually labeled the boundaries of the three cortical layers. We estimated the layer thicknesses from the binary mask obtained from cortical layer segmentation using an algorithm from our previous work¹⁷. We chose two gyral crest regions and a sulcus region indicated by the white boxes in the binary mask image. The bottom panel displays the box plot of the local layer thickness statistics in gyrus and sulcus regions. We observed a similar pattern of variation in layer thickness for layer IV, V, and VI in the sulcus, gyrus and the entire cortical regions. The median local thickness of layer IV, V, and VI were 300 μm , 540 μm , and 480 μm respectively. We also observed a significant reduction in layer thickness in all three layers in the sulcus regions compared to the gyrus regions, in agreement with the literature^{44,45}. The median thickness

of layer IV, V, and VI were 410 μm , 630 μm , and 580 μm respectively in the gyrus regions, and were 250 μm , 370 μm , and 310 μm respectively in the sulcus regions.

Volumetric digital staining on cubic centimeter-scale brain tissue

Next, we showcase volumetric staining on cubic centimeter-scale brain tissue enabled by our technique that combines S-OCT and DS. Our technique significantly reduces tissue distortion and misalignment during the 3D reconstruction process suffered by the traditional 3D pathology technique. We demonstrate 3D DS on a 4 cm \times 5 cm \times 1.2 cm brain tissue block that was not used for training our DS model. We show that our method can preserve the intricate 3D brain structures in both gray matter and white matter regions. Moreover, we visualize the 3D vessel network in the white matter.



In Fig. 5a, we present a 3D visualization of the DS output on the whole tissue block in the top panel. The DS model takes as input a z-stack of around a hundred slices of OCT-SC images. Each OCT-SC slice, which has a size of $4\text{ cm} \times 5\text{ cm}$, is processed separately and fed to the DS model. The DS output images are then directly stacked along the z-axis to create the digitally stained volume. Consistent with the 2D results, the 3D DS volume generates white and dark-brown colors that correspond to gray matter and white matter regions respectively. We can also observe a smooth transition of these gray matter and white matter boundaries along the z direction, which reflects the preservation of 3D geometries of the brain structures. In Fig. 5b, we display several orthogonal cross-sectional views of the DS volume. The overall color tone and contrast variations match with the 2D results in Fig. 3. Small white blobs and tubes within the white matter region indicate the vessel space. These results are consistent with 2D DS results that have been verified with PS references, and partly confirm the generalization ability of our DS model on unseen large-scale brain samples. Moreover, the X-Z cross section also shows several continuous features along the depth, such as intricate brain folding structures, double-band cortical layers, and small tubular vessels. This again illustrates the 3D geometry preservation feature of our DS technique.

To further illustrate the ability of our DS technique to preserve the 3D geometry of mesoscale brain structures, we present a 3D visualization of a centimeter-scale network of vessel space which is not visible in 2D PS images. Besides the gray matter and white matter contrast, our DS volume also shows several continuous white tubular structures corresponding to blood vessels in the top panel of Fig. 5a. In the bottom panel of Fig. 5a, we show the segmented DS volume displaying only the white matter region, where the white tubular structures are more prominent and not masked by the gray matter. In Fig. 5c, we highlight two regions in yellow and green boxes. The vessel spaces in those regions are rendered with more transparency and reveal the branching and connectivity of the vessel network. On the right panel of Fig. 5c, three orthogonal maximum intensity projections (MIP) of the DS volume further demonstrate the preservation of the 3D vessel structures. We note that the axial continuity of our DS volume is currently limited by the axial resolution ($150\text{ }\mu\text{m}$) imposed by our SC fitting model, which we aim to improve in the future. To quantify the improved 3D geometry preservation compared to traditional physical staining, we performed quantitative analysis in Supplementary Section 15 and Fig. S17. Being able to image brain samples as large as $4 \times 4 \times 1\text{ cm}^3$ ³⁸, we can easily extend the aforementioned analysis to large brain areas

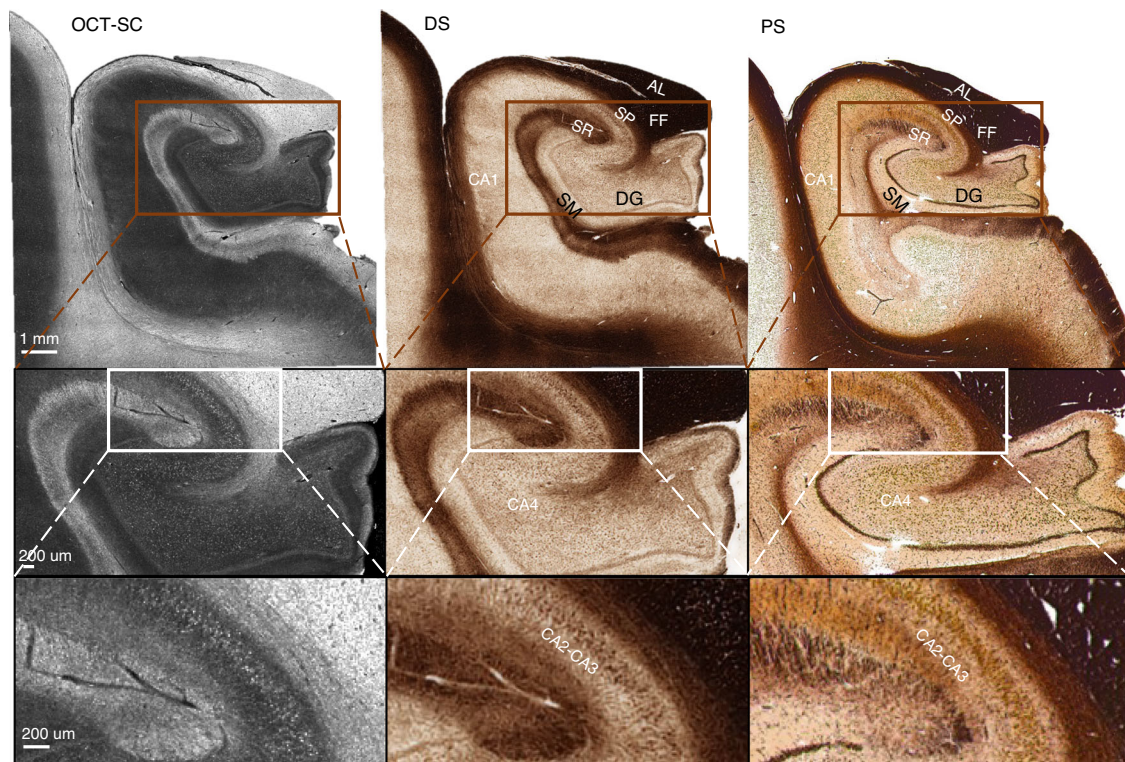


Fig. 6 DS-OCT generalization performance on an unseen hippocampus tissue slice. Examples of OCT-SC, DS, and PS images (of adjacent sections) on one sample from the Hippocampus region are shown. SP: Stratum Pyramidale; AL: Alveus; FF: Fimbria Fomix; SR: Stratum Radiatum; SM: Stratum Moleculare; DG: Dentate Gyrus; CA: *Cornu Ammonis*. The shown slice comes from an unseen subject entirely independent of training and testing subject set

with uniform and enhanced contrasts, which could greatly improve the throughput of brain anatomy study.

Generalization to unseen anatomical regions

To further demonstrate the generalization capability of our trained DS model, we conducted a pilot study on different anatomical regions that were imaged by a different S-OCT setup not seen during training. We used the same fitting model to generate the OCT-SC image in Fig. 6, which shows a sample from the hippocampus region acquired by a different S-OCT setup. Since our SC fitting model extracts an intrinsic tissue property and is relatively insensitive to variations in hardware platforms and sample conditions, it ensures the robustness of our DS method. The DS image is inferred by directly inputting the OCT-SC to the previously trained model. Figure 6 shows the OCT-SC and DS images, and the reference PS image of an adjacent section from left to right. We roughly aligned the field of views of the DS and PS images using a rigid transformation. On a large scale, the DS process successfully transforms the image contrast to match the anatomical structures found in the PS image. By comparing with the anatomy of hippocampus⁴⁶, we can identify the alveus (AL) and/or fimbria fomix (FF) layer at

the top, the stratum pyramidale (SP) layer beneath them, and the stratum radiatum (SR), stratum moleculare (SM) and the dentate gyrus (DG) layers that encase the *Cornu Ammonis* areas (CA1-CA4) of dense neurons. Importantly, in CA1-CA4 areas, we found bright spots in OCT-SC images, which are transformed to brown spots in the DS images. These structures correlate strongly with the brown spots seen in the PS image and are likely individual neuron somas. More examples of generalization results can be found in Supplementary Section 8 and Figure. S8.

Such generalization agrees with our previous work that discovered a universal correlation between optical scattering and myelin density across the human brain²¹. This suggests that a DS-OCT model, even if trained on limited regions of the human brain, may be effectively employed in other unseen regions. This significantly decreases the training effort compared to those that rely on transfer learning.

Discussion

In summary, we developed a novel semi-supervised learning technique for DS of OCT images for large-scale volumetric visualization and analysis on human brain tissue samples. Our technique works by integrating

label-free S-OCT imaging and an advanced deep learning DS model. The S-OCT enables imaging of cubic centimeter-scale brain tissues and preserves complex 3D tissue geometry across sections. Our semi-supervised learning method bypasses the need for paired unstained and stained images and can achieve high-quality DS using a limited amount of weakly paired image data for model training. Our deep learning model is built on an unsupervised CUT model backbone, which is augmented with two auxiliary tasks. The pseudo-supervised module reduces the data requirement for model training by exploiting the correlation between the OCT-SC and the OD of Gallyas silver stain. The unsupervised cross-modality image registration module exploits the structural information between the adjacent tissue sections. By working with a fitted tissue property, namely the scattering coefficient, from the raw OCT measurement as the input to the deep learning model, it greatly enhances the uniformity and generalizability of the DS results. This is highlighted by our volumetric DS result on cubic centimeter-scale brain tissue block and on unseen anatomical regions from different OCT systems. We believe our OCT DS technique is a promising solution for large-scale human brain imaging for comprehension characterization of brain structure across scales.

Our work introduces two significant innovations. Firstly, we present a novel deep learning model tailored for weakly-paired DS. While supervised and unsupervised DS methods are well-established for *pairable* data affected by mild geometric distortions from physical staining, our research addresses a critical challenge: the absence of pairable ground truth data in our specific context. This challenge arises because physical stained sections, despite being adjacent, may not correspond precisely to the same z-plane as OCT images, which are constrained within an imaging depth of 150 μm , while stained sections are 50 μm thick. This inherent content mismatch is prevalent in various biomedical imaging scenarios where different modalities are compared. Our approach capitalizes on existing data resources without altering current imaging pipelines, pioneering a new formulation for the weakly-paired problem setting and proposing a novel methodology to address this fundamental issue in biomedical research where paired data are unattainable.

Secondly, we introduce an enhanced modality—digitally stained OCT—for volumetric brain imaging. Beyond merely advancing deep learning model capabilities, we validate the utility of the DS technique through proof-of-concept applications. We introduce new evaluation pipelines and metrics tailored specifically for the Gallyas silver stain, crucial for neuroimaging in neurodegenerative disease research. Our study demonstrates the advantages of integrating S-OCT with DS through

preliminary histopathology-based analyses, showcasing the potential of this combined approach.

We envision that our deep learning framework holds great potential for a wide range of applications in the field of DS. There is a growing demand for exploring semi-supervised learning approaches to effectively harness the wealth of information contained in unpaired or weakly paired biomedical images. Obtaining pairs of images with labels and without labels can be a challenge in many biomedical contexts. However, it is often easier to obtain images of samples with slight distortions or adjacent sections. To leverage these types of datasets, our method leveraged a novel inverse mapping technique, going from stained images to label-free modalities, and generated pairs of images that were pixel-aligned to serve as augmented supervision. Furthermore, we introduced a novel cross-modality registration algorithm to correct for sample distortions and account for the complex geometries of the samples. As a result, our enhanced semi-supervised learning framework facilitates more straightforward training on datasets that may be naturally acquired from routine staining experiments, even when those datasets are only weakly paired. In essence, incorporating semi-supervised methods can significantly enhance the efficiency of the “data collection-training-validation” cycle in the development of DS models.

We discuss several key limitations that impact the quality of S-OCT images and the corresponding DS method. The first limitation arises from the data processing pipeline of OCT imaging. Coherent scattering results in speckle noise, which appears as randomly distributed fine-grained dark or white spots in both OCT and the derived SC images. These speckle artifacts do not necessarily correspond to actual cortical structures in PS images, as shown in Fig. 3, Supplementary Fig. S6 and Fig. S15. Consequently, visualizing and digitally staining small vessels, capillaries, and fine axonal fiber structures become challenging. In terms of evaluation pipeline, when comparing DS and PS results side-by-side, the inherent content mismatch, lack of z-alignment and contrast loss due to speckle noise all contributed to the inconsistencies of features such as blood vessels. Moreover, the current $\sim 20\ \mu\text{m}$ resolution of our OCT-SC data is insufficient to resolve delicate structures like single neurons, which are typically discernible in traditional histology⁴⁷. To address this limitation, future work can optimize the OCT-SC processing pipeline using deep learning techniques to enhance imaging quality. For example, self-supervised learning algorithms for speckle suppression can be developed by utilizing a customized blind-spot denoising network and a speckle statistics model⁴⁸. Enhancing the resolution of SC can be explored by using a deep learning model similar to ref. ⁴⁹, which can learn a more accurate and robust fitting model without relying on local-

averaging. These improvements can improve the robustness and resolution of our method, allowing for the capture of finer neuronal structures. The second limitation relates to stitching artifacts that our current DS model cannot fully correct, thereby affecting the quality of the WSI image, as observed in Supplementary Fig. S8. To address this issue, incorporating a structural prior constraint into our DS training framework can potentially yield better correction of these artifacts. The final limitation concerns the imperfect registration component in our DS model. The depth range used for fitting the SC (150 μm) is larger than the physical sectioning thickness of the PS images (50 μm). Furthermore, sample destruction during staining process can introduce content mismatches. However, our registration network only corrects for global-scale geometric distortions between adjacent sections and does not account for potential content mismatches between weakly-paired images. Consequently, the registration process fails to generate pixel-aligned image data, as shown in Supplementary Fig. S3. To tackle this issue, further improvements to the deep learning framework may consider methods to address content mismatches.

Due to these limitations, our DS-OCT technique cannot fully replace traditional physical staining in terms of interpretability. However, the proposed modality offers a unique combination of the data uniformity and 3D imaging capability of S-OCT with the interpretability associated with traditional staining, as illustrated in Supplementary Fig. S1. By employing deep-learning-based DS, we enhance the interpretability of S-OCT through learned properties such as local color mapping and global contrast enhancement. Additionally, we leverage the quantitative and distortion-free nature of OCT scattering coefficients to mitigate the appearance variability and 3D geometric distortions that are inherent in the traditional staining process.

Our current study, however, is based on a limited dataset in terms of both samples and slices, leading to preliminary generalization results. We plan to conduct additional experiments and collect a more diverse dataset to further enrich our findings and refine our method in the future. It is worth noting that our training and testing images comprise a mix of normal control and neurodegenerative human brain samples, which hinders the model's ability to learn the distinctions between normal and diseased brain images. To expand our work towards distinguishing between normal and diseased cases, one needs to acquire images from a larger set of brain samples for both conditions. Additionally, we plan to incorporate multi-modality input, such as polarization information, into our DS model to increase the imaging sensitivity to birefringence structures, including myelin fibers^{17,19}. Another promising modality we aim to integrate with the

S-OCT is two photon microscopy, which allows imaging of small vessels and myelin fibers based on auto-fluorescence contrast with reduced noise and improved resolution³⁸.

Materials and methods

Serial-sectioning OCT (S-OCT)

The S-OCT microscope was described previously³⁸. We used a swept light source (AxsunTech) with 100 kHz swept rate, a central wavelength of 1310 nm, and a spectral full width half maximum of 110 nm, yielding an axial resolution of 5.6 μm in brain tissue (mean refractive index $n = 1.4$). We used a free-space interferometer and quarter wave plate (QWP) to illuminate the sample with circularly polarized light and used two balanced detectors for measuring orthogonally polarized reflection light. A variable retarder (VR) placed in the sample arm was used to compensate for the system birefringence and to recover precise measurement of sample birefringence. To sample the spectrum in even- k space, we input the k -clock of the light source into a high-speed digitizer (ATS9350, AlazarTech), afterwards real-time FFT was carried out using a Graphic Processing Unit (RTX4000, NVIDIA), and the spatial-domain data was trimmed to only save the first 1 mm depth. The post-objective power was measured to be 3.7 mW, achieving a 95 dB SNR in both polarization channels. We used $1 \times 1 \text{ mm}^2$ FOV with 3 μm lateral step size and 30% overlap between tiles. The sample was mounted on XYZ motorized stages which translated the sample in the X-Y plane to image the whole surface as well as in the Z plane between the vibratome and objective. After block-face imaging, a custom vibratome cut off the 50 μm slices with 0.3 mm/s cutting speed and 3000 rotations per minute (RPM) blade vibrating frequency.

Optical properties estimation with S-OCT

Tissue optical properties were extracted by following a previously established procedure to analyze the reflectance intensities of OCT using a nonlinear fitting method^{11,12}. To summarize, spatial parametrization is first applied to the confocal parameter across a 3D OCT image to constrain and reduce the degrees of freedom in the nonlinear coefficient fitting problem, resulting in improved confidence in the estimated optical properties of the sample. Afterwards, a nonlinear least-squares solver is used to estimate the back-scattering and scattering coefficients from the nonlinear reflectance-vs-depth over about 150 μm depth. All curve fitting was performed in MATLAB. After extracting the optical properties for each image tile, the tiles were stitched using the coordinates generated during the volumetric reconstruction with ImageJ software⁵⁰. The resulting image pixel size is 12 μm due to a 4×4 downsampling.

Sample preparation

A total of 18 subjects contributed post-mortem samples to this study, which were grouped based on the originating subject. 15 individual subjects contributed 15 samples that were used in the training and testing phases, with each subject providing one sample. The remaining 3 subjects contributed 6 samples that were used in the pilot generalization study.

For the training and testing phase, we used the 15 samples obtained from the Boston University Alzheimer's Disease Research Center (ADRC) brain bank. The subjects from whom these samples were derived from had a mean age of 78.8 years, comprising 2 females and 13 males. These samples included five cases with stage VI Alzheimer's disease (AD), five cases with stage III and IV Chronic Traumatic Encephalopathy (CTE), and five age-matched normal control cases. Each of the 15 samples corresponded to one OCT imaging volume, which was scanned by the OCT machine and subsequently sliced to yield 35 slices (9 for training and 26 for testing). The 9 training slices were drawn from 7 samples, while the 26 testing slices came from 12 samples, with an overlap of 4 samples between the two sets. To ensure slice independence and adequate representation across the thickness of the tissue, we selected one slice per millimeter for this study. Doing so ensured that each slice in the entire training and testing set was visibly distinct and statistically de-correlated. Our pre-processing involved non-overlapping patch cropping on the WSIs to further make sure that the training and testing data patches remained independent. This process is further detailed in the analysis in Supplementary Section 17 and Figure. S19.

For the pilot generalization study, we used OCT data from 6 samples obtained from 3 human brains, which were entirely independent of the training and testing subjects. These samples were collected at the Massachusetts General Hospital Autopsy Suite and encompassed various brain regions, including the cerebellum, hippocampus, somatosensory cortex, superior frontal cortex, and middle temporal area 21. The subjects from whom these samples were obtained had no history of neurological deficits and had a mean age of 53.5 ± 12.0 years, comprising two males and one female.

All samples were fixed by immersion in 10% formalin for at least two months. The post-mortem interval did not exceed 24 h. Prior to imaging, the samples were washed in 1X phosphate buffered saline for a month to remove residual fixation agents and then embedded in 4.5% agarose for tissue support⁵¹. During embedding, the brain blocks were warmed to 65 °C to allow sufficient penetration of agarose into the deep sulcus. During imaging, the brain tissue blocks were mounted in a water bath filled with Deionized (DI) water. The DI water was changed every day to remove the debris from cutting that could

degrade the OCT image quality. Following data collection, the tissue slices were stored in 1X PBS with an anti-bacterial agent (sodium azide) at a temperature of 4 °C. To maintain the sequence of the slices, each slice was stored in an individual glass vial.

Gallyas silver staining and imaging

A total of 35 brain slices were obtained from 15 samples for our study. To ensure anatomical diversity, at least two slices were taken per sample, with each slice being separated in depth by 1 mm. These slices had a thickness of 50 μm and were mounted onto gelatin-coated slides. Gallyas staining protocol, as described by Pistorio², was then employed to process the samples. Modifications were made to the impregnation and bleaching time to accommodate the increased thickness of the samples. Due to the limit of experiment container size, we split the total 35 slices into two batches: the first batch contains small samples that can fit onto smaller slides ($75 \times 25 \text{ mm}^2$), while the second batch contains wider samples mounted on bigger slides.

Following the staining process, the samples were captured in brightfield mode using a $10\times$ objective ($\text{NA} = 0.4$) and an RGB camera. We utilized the VS-120 slide scanner designed for $75 \times 25 \text{ mm}^2$ slides for this purpose. The exposure time was set at 1.73 ms, and the pixel size was 0.7 μm with a $1 \times 1 \text{ mm}^2$ FOV. For wider samples from the second batch, imaging was conducted using the BZ-X microscope under similar settings with image pixel size of 1.9 μm . The resulting images can be opened in Olympus Olyvia software and exported as TIFF images for further processing.

Image processing

Our image dataset consists of two types of images: PS images from the slide scanner and OCT-SC images computed from S-OCT. Our anatomist experts visually inspected the PS images and graded the staining quality for the first batch. Out of the first batch staining results, we selected 9 slices that are graded as ideally-stained for training our DS model. The rest 26 slices are a mix of ideally-stained and less well-stained slices, since they contain results from the second staining batch. The PS WSIs had different sizes depending on the tissue sample, but they were around the median scale of $36 \text{ mm} \times 48 \text{ mm}$ with the pixel size of 0.7 μm /1.9 μm depending on the batch. To generate the weakly-paired training dataset, we manually paired the PS images with the OCT-SC images that had the most similar appearance. Since the sectioning thickness (50 μm) of PS samples did not match the fitting thickness used for OCT-SC images (150 μm) and the depth information of PS samples was not recorded, we can only pair the PS with the closest adjacent OCT-SC image sample by qualitatively assessing the similarity of

tissue features. We then downsampled the PS images using bicubic interpolation to match the $12\ \mu\text{m}$ pixel size in OCT-SC images. We also cropped or padded the PS images to have the same image size as the corresponding OCT-SC images, which was around 3000×4000 pixels for each sample. We performed this procedure on all PS images when we compared them with the OCT-SC images side-by-side in our results.

The PS images undergo several preprocessing steps to minimize the effects of sample and staining variations before they are used for training. The preprocessing steps include background removal, intensity normalization and color transfer. The background removal eliminates the unwanted image artifacts in PS image and is done by interactive image segmenter in MATLAB. The intensity normalization adjusts the PS images to balance the varying illumination levels across different imaging experiments. The brightest pixel (I_r, I_g, I_b) is used to estimate the illuminant color and the image is scaled by the constant ($1/I_r, 1/I_g, 1/I_b$) for each color channel, followed by a range normalization to map the overall image value range to $[0, 1]$. The color transfer uses Reinhard method⁵² to standardize the staining color variations among experiment, sample and imaging conditions given a target PS image with a relatively ideal staining as reference.

The OCT-SC images obtained from the fitting algorithm show some artifacts mainly in the background areas and near the sharp boundaries of the vessel regions, because the algorithm assumes a constant SC value for the $150\ \mu\text{m}$ imaging thickness¹¹. To reduce the background noise and correct the over-smoothed values near the vessel edges, the OCT-SC images are further processed by several steps. First, the background is removed by applying a histogram-based thresholding method using the triangle algorithm⁵³, followed by a sequence of smoothing morphological operations such as erosion, small object removal and dilation. Next, the pixels with zero values in the masked image are identified as defective and are replaced by the local median. Then, the edges of the vessel regions are detected using a difference-of-Gaussian (DoG) filter and thresholding. Finally, the outlier regions with small values compared to the local maximum are segmented and combined with the edge mask. The combined mask is smoothed by similar morphological filters, and the values in the mask are replaced by the local maximum. The preprocessing pipeline is implemented in Python using the basic filters and morphological operators from scikit-image package⁵³.

To generate the training image dataset, we used PyTorch to create a parallel processing module that can split the WSIs of different image sizes into smaller patches during training on the fly. This allows us to dynamically update the intermediate image tensors that can be input to different parts of deep learning models to train at

different image scales. The WSIs dataset with different sizes can then be directly handled by a custom data loader for standard-size tensor operation. We apply histogram equalization to the WSIs X to normalize intensity distribution before feeding them into G . This operation is consistent with the pre-processing of the pseudo-supervised learning module (see details in the following section). We first pad the WSI to the size of multiple integers of patch size, and then use the tensor unfolding method in PyTorch to cut the image tensor using a sliding window into smaller tensors stacked in the batch dimension. The inverse stitching operation is done similarly using the tensor folding methods.

For creating a 3D visualization of the DS images that show the volumetric digital staining results, we change the white-color background of the DS images to black, so that only the sample region is visible. This is done by converting the DS color images to grayscale and applying a triangle method threshold to select the foreground pixels. Then, a morphology smoothing operation is performed to remove any noise or artifacts. To extract the white matter masks from the DS grayscale images for highlighting the white matter regions in the sample, we use a histogram thresholding method based on the minimum method⁵³ and apply another morphology smoothing operation. The pixels that are not part of the white matter masks are set to zero, and the resulting images are stacked in a volume for 3D visualization. The 3D viewer in ImageJ⁵⁰ is used to display the volume. More details on the image processing procedures are provided in Supplementary Section 9 and Fig. S9.

Semi-supervised deep learning framework

The proposed framework combines generative adversarial learning, contrastive learning, pseudo-supervised learning based on self-generated image pairs based on a biophysical model, and unsupervised cross-modality image registration.

We denote the OCT-SC images as X and the PS images as Y . The main framework consists of a DS network G and a registration network R . The DS network G transforms grayscale OCT-SC images X into color images that resemble the color and contrast of PS images Y . The registration network R takes pairs of unaligned images X and Y as input and outputs a deformation field $\phi = R(X, Y)$ that can be applied to resample and register Y to X . We use an auxiliary discriminator network D to enforce structural similarity between the output DS and reference PS images by adversarial learning. We also apply contrastive learning to ensure structural consistency between the input OCT-SC and output DS images using a fully connected network f .

Our framework operates on two different image scales: WSI scale (denoted by upper case letters X, Y) and image

patch scale (denoted by lower case letters x, y). R is trained on WSIs, which have a size of about 3000×4000 pixels. G, D, f are trained on image patches, which have a size of 512×512 pixels. We design an efficient image processing module to either split (X, Y) into patches (x, y) or stitch patches back to WSIs, as detailed in the Image Processing section. The CUT framework³³ is used to jointly train the networks G, D , and f during the training phase. Additionally, G undergoes a pseudo-supervised training scheme and an alternating training process with R , which are explained below.

The objective of the adversarial learning module is to enhance the perceptual similarity between the DS output $G(x)$ and the target modality PS images y . This is achieved by using an auxiliary discriminator D . The role of D is to learn to differentiate between the desired modality y and the generated images $G(x)$. During the training of D , the PS images y are assigned the label 1, indicating that they are “true” images. On the other hand, the generated images $G(x)$ are assigned the label 0, indicating that they are “false” images. The least-squares generative adversarial network (GAN) loss $L_{\text{GAN}}(D)$ is employed to measure the extent to which D 's outputs align with the binary labels assigned to both y and $G(x)$. This loss function is minimized when D becomes proficient at distinguishing between y and $G(x)$. Conversely, when training G , the $L_{\text{GAN}}(G)$ loss is utilized to promote the fidelity of the generated images $G(x)$. Minimizing this loss prompts G to effectively deceive the discriminator D . The training process alternates between two steps: first, G is fixed while D is updated using the $L_{\text{GAN}}(D)$ loss, and then D is fixed while G is updated using the $L_{\text{GAN}}(G)$ loss:

$$L_{\text{GAN}}(D) = E_y[(D(y) - 1)^2] + E_x[D^2(G(x))] \quad (1)$$

$$L_{\text{GAN}}(G) = E_x[(D(G(x)) - 1)^2] \quad (2)$$

The contrastive learning module ensures that the image structures and content present in x is preserved when it is translated to $G(x)$. We implement G with a ResNet model and treats the first half of the ResNet layers as the encoder and the remaining layers as the decoder. The encoder G_{enc} transforms images from both domains into a common latent space, and the decoder G_{dec} generates translated images from latent vectors. To formulate the multi-layer patch-wise contrastive loss, we adopt the approach in (32) to sample the encoded feature maps from both x and $G(x)$. Each layer and spatial location in the feature map stack corresponds to a patch of the input image that covers the corresponding receptive field. We extract multiple layers of the encoded feature maps, randomly sample the spatial locations and apply a fully connected network f to obtain a stack of latent features $z_{s,l} = f(G_{\text{enc}}^{s,l}(x))$, where s is the spatial index within $[1, S]$ and l

is the selected layer within $[1, L]$. We do the same processing on image $G(x) : \hat{z}_{s,l} = f(G_{\text{enc}}^{s,l}(G(x)))$. Then we compute a PatchNCE loss using a cross-entropy contrastive loss:

$$L_{\text{PatchNCE}}(G, f, x) = E_x \sum_{l=1}^L \sum_{s=1}^S \log \left(\frac{\exp(z_{s,l} \cdot \hat{z}_{s,l})}{\sum_{t=1}^S \exp(z_{s,l} \cdot \hat{z}_{t,l})} \right) \quad (3)$$

This loss function encourages the latent representations of image patches from x and $G(x)$ that belong to the same spatial location to have similar content to be close in the feature space, while pushing away the representations of patches that are uncorrelated or have different content. By this internal negative sampling scheme in the feature space, the model learns to contrast positive and negative pairs of patches based on their content similarity, which maximizes the mutual information between the input image x and the output image $G(x)$. This provides a self-supervised signal for preserving the content of the image during the transformation.

The training procedure for pseudo-supervised learning is formulated as a pixel-wise loss function that minimizes the discrepancy between the digital stained OD images $G(\text{OD}(Y))$ and the physical Gallyas-silver stain (PS) images Y . This loss function aims to guide G to learn a mapping that translates images from the OD modality to the PS modality. By doing so, it provides a “proxy supervision” for learning the mapping from OCT-SC modality to the PS modality. To facilitate this training, we first compute the OD of image Y by

$$\text{OD}(Y) = -\frac{1}{3} \sum_{c=R,G,B} \log_{10} Y_c \quad (4)$$

Subsequently, we extract patches $\text{OD}(y)$ and y from the processed WSIs and employ an auxiliary pseudo-supervised loss, defined as:

$$L_{\text{Pseudo}}(G) = E_y \|G(\text{OD}(y)) - y\|_1 \quad (5)$$

However, there exists a mismatch in the intensity values between X and $\text{OD}(Y)$. This domain gap between the input modalities hinders the model's direct generalization on X if it is solely trained on pairs of $\text{OD}(Y)$ and Y . To address this issue, we first apply histogram equalization to the WSIs of $\text{OD}(Y)$ and X before feeding them into G . This normalization step aims to align the distribution of intensity range. However, we found that this transformation alone is insufficient in mitigating the domain gap. As a result, this learning module is further combined with the adversarial learning module in the CUT backbone to mitigate the domain gap between OCT-SC and OD.

The cross-modality image registration module is trained in two stages. In the first stage, we pre-train the registration network R on WSIs of X , Y and $OD(Y)$. The registration network R takes weakly-paired X and Y as input and predicts a deformation field $\phi = R(X, Y)$ that indicates the pixel-wise displacement vectors needed to perform the non-rigid transformation. To formulate a cross-modal self-supervised registration loss L_{reg}^I , we use $OD(Y)$ as a surrogate of Y and exploit its correlation with the input OCT-SC image X . By minimizing the difference between the registered $OD(Y)$ and X , we indirectly learn the deformation between Y and X . This training is enabled by a differentiable resampling layer that performs image warping denoted by \circ . We also add a total variation (TV) regularization term to encourage the smoothness of the learned deformation field. The registration loss during this pre-training stage is computed at the WSI scale as follows:

$$L_{reg}^I(R) = E_{X,Y} \|X - \phi \circ OD(Y)\|_1 + \|\phi\|_{TV} \quad (6)$$

where $\|\phi\|_{TV}$ is the total variation norm calculated as:

$$\|\phi\|_{TV} = \sum_{ij} \sqrt{|\phi_{i+1} - \phi_{ij}|^2 + |\phi_{ij+1} - \phi_{ij}|^2} \quad (7)$$

In the second fine-tuning stage, we train R and G in an alternating and collaborative manner. The purpose of fine-tuning R is to provide pixel-wise weak-supervision between the registered Y and the DS image $G(x)$, which in turn helps to fine-tune the DS network G . Using the coarsely trained G , we can produce $G(x)$ that has the same image modality as the PS image Y and use a pixel-wise loss function to perform training. We implement the following scheme for alternating training. When we fix G , we train R by comparing the registered PS image Y and the DS image $G(X)$ at the WSI scale using the loss function

$$L_{reg}^{II}(R) = E_{X,Y} \|G(X) - \phi \circ Y\|_1 + \|\phi\|_{TV} \quad (8)$$

When we fix R , we crop the intermediate registered WSI $\phi \circ Y$ into patches $\phi_{y \circ y}$ and train G at the patch scale by comparing the registered PS image patch and the DS image patch $G(x)$ using the loss function

$$L_{reg}^{II}(G) = E_{x,y} \|G(x) - \phi_{y \circ y}\|_1 \quad (9)$$

Our models are trained on BU Shared Computing Cluster (SCC) with one Nvidia Tesla P100 GPU. Training time is 2.87 h for registration network pre-training and 13.6 h for whole model training. Additional details about the deep learning framework and individual model architectures are provided in Supplementary Sections 10, 11 and Figs. S10, S11 and S12. A non-learning “DS”

method based on simple inverse color mapping is also constructed and compared to our DL-based approach in Supplementary Section 14 and Fig. S16.

Image analysis

The layer differentiation analysis is primarily performed using the open-source ImageJ software package. The line profiles are computed by selecting the rectangular region in the center region of interest (ROI) and aggregating the intensity value along the horizontal direction. Those profiles are then normalized to $[0, 1]$ by their individual value range for visual comparisons. The cortical layer boundaries are manually annotated by identifying the local maxima and edges according to refs. ^{40,41}. The layer segmentation on the larger ROI is performed by manual annotation on layer IV, V, and VI. We used the built-in local thickness estimation function to generate the local thickness map and calculated the box plot for the thickness distribution using Matlab. Two Gyrus crest ROIs and one Sulcus ROI are manually selected. Additional details about the analysis methods for the myelin fibers and vessel quantification are provided in Supplementary Section 13 and Fig. S14.

Acknowledgements

The authors acknowledge funding support from: National Institutes of Health grant R01 EY032163 (S.C., L.T.). National Institutes of Health grant U54 NS115266 (A.C.M.). National Institutes of Health grant P30 AG072978 (A.C.M.). National Institutes of Health grant U19 AG068753 (A.C.M.). National Institutes of Health grant R01 NS125307 (D.L.R.). National Institutes of Health grant R01 AG075727 (D.L.R. and I.J.B.). National Institutes of Health grant RF1 AG062831 (D.L.R.). Boston University Kilachand Fund Award (I.J.B., D.L.R., D.A.B., and L.T.). National Institutes of Health grant R00 EB023993 (H.W.). National Institutes of Health grant R01 NS128843 (H.W.). National Institutes of Health grant U01 MH117023 (S.C., A.N., D.A.B.).

Author details

¹Department of Electrical and Computer Engineering, Boston University, Boston, MA 02215, USA. ²Department of Electrical Engineering and Computer Sciences, University of California, Berkeley, CA 94720, USA. ³Department of Biomedical Engineering, Boston University, Boston, MA 02215, USA. ⁴Department of Computer Science, Boston University, Boston, MA 02215, USA. ⁵Boston University Alzheimer's Disease Research Center and CTE Center, Boston University School of Medicine, Boston, MA 02118, USA. ⁶Department of Neurology, Boston University School of Medicine, Boston, MA 02118, USA. ⁷VA Boston Healthcare System, U.S. Department of Veteran Affairs, Boston, MA 02130, USA. ⁸Department of Pathology and Laboratory Medicine, Boston University School of Medicine, Boston, MA 02118, USA. ⁹Department of Anatomy & Neurobiology, Boston University School of Medicine, Boston, MA, USA. ¹⁰Department of Radiology, Athinoula A. Martinos Center for Biomedical Imaging, Massachusetts General Hospital, Boston, MA 02129, USA. ¹¹Neurophotonics Center, Boston University, Boston, MA 02215, USA

Author contributions

L.T., D.A.B., and I.J.B. conceived the original idea of this work. H.W. provided initial OCT data and processing algorithms for prototyping. D.L.R. provided experimental supervision and guidance, chemical material, and laboratory support for Gallyas silver stain. A.C.M. provided valuable brain samples and initial Gallyas silver stained image data for prototyping. Shiyi C. constructed the algorithmic pipeline for image processing, neural network design, training and testing, image analysis and results evaluation, and performed Gallyas silver staining (GSS) experiment with A.N. Shuaibin C. constructed the S-OCT

hardware setup, performed brain sample sectioning and imaging experiment, constructed scattering coefficient fitting and data preprocessing algorithms. Y.L. provided innovative ideas on modifications and refinement on the computational framework and performed extensive image data analysis. A.N. performed the GSS experiment with Shiyi C. and completed bright field imaging and image acquisition. S.L. constructed and optimized CUT and FastCUT neural networks for baseline model comparison. Y.W. and J.Z. constructed and optimized CycleGAN network for baseline model comparison. All authors contributed to the writing of the paper and insightful discussions on the result analysis.

Data availability

We have open sourced our codebase with training/testing script and pre-trained model weights on our GitHub repository: <https://github.com/bu-cisl/DS-OCT>. All data needed to evaluate the conclusions in the paper are present in the main text or the supplementary information. Additional data are available upon reasonable requests to the authors.

Conflict of interest

The authors declare no competing interests.

Supplementary information The online version contains supplementary material available at <https://doi.org/10.1038/s41377-024-01658-0>.

Received: 4 March 2024 Revised: 29 September 2024 Accepted: 11 October 2024

Published online: 20 January 2025

References

- Herculano-Houzel, S. The remarkable, yet not extraordinary, human brain as a scaled-up primate brain and its associated cost. *Proc. Natl Acad. Sci. USA* **109**, 10661–10668 (2012).
- Pistorio, A. L., Hendry, S. H. & Wang, X. Q. A modified technique for high-resolution staining of myelin. *J. Neurosci. Methods* **153**, 135–146 (2006).
- Kuninaka, N. et al. Simplification of the modified Gallyas method. *Neuropathology* **35**, 10–15 (2015).
- Amunts, K. et al. BigBrain: an ultrahigh-resolution 3D human brain model. *Science* **340**, 1472–1475 (2013).
- Yushkevich, P. A. et al. 3D mouse brain reconstruction from histology using a coarse-to-fine approach. *Proc. 3rd Biomedical Image Registration* (Utrecht: Springer, 2006).
- Osechinskiy, S. & Kruggel, F. Slice-to-volume nonrigid registration of histological sections to MR images of the human brain. *Anat. Res. Int.* **2011**, 287860 (2011).
- Min, E. et al. Serial optical coherence microscopy for label-free volumetric histopathology. *Sci. Rep.* **10**, 6711 (2020).
- Cao, R. et al. Label-free intraoperative histology of bone tissue via deep-learning-assisted ultraviolet photoacoustic microscopy. *Nat. Biomed. Eng.* **7**, 124–134 (2023).
- Zhang, Y. et al. Three-dimensional label-free histological imaging of whole organs by microtomy-assisted autofluorescence tomography. *iScience* **25**, 103721 (2022).
- Sun, Y. et al. Real-time three-dimensional histology-like imaging by label-free nonlinear optical microscopy. *Quant. Imaging Med. Surg.* **10**, 2177190–2177190 (2020).
- Wang, H. et al. Characterizing the optical properties of human brain tissue with high numerical aperture optical coherence tomography. *Biomed. Opt. Express* **8**, 5617–5636 (2017).
- Yang, J. R. et al. Improving the characterization of ex vivo human brain optical properties using high numerical aperture optical coherence tomography by spatially constraining the confocal parameters. *Neurophotonics* **7**, 045005 (2020).
- Magnain, C. et al. Colocalization of neurons in optical coherence microscopy and Nissl-stained histology in Brodmann's area 32 and area 21. *Brain Struct. Funct.* **224**, 351–362 (2019).
- Yang, J. R. et al. Volumetric characterization of microvasculature in ex vivo human brain samples by serial sectioning optical coherence tomography. *IEEE Trans. Biomed. Eng.* **69**, 3645–3656 (2022).
- Magnain, C. et al. Blockface histology with optical coherence tomography: a comparison with Nissl staining. *NeuroImage* **84**, 524–533 (2014).
- Magnain, C. et al. Optical coherence tomography visualizes neurons in human entorhinal cortex. *Neurophotonics* **2**, 015004 (2015).
- Wang, H. et al. as-PSOCT: volumetric microscopic imaging of human brain architecture and connectivity. *NeuroImage* **165**, 56–68 (2018).
- Liu, C. J. et al. Visualizing and mapping the cerebellum with serial optical coherence scanner. *Neurophotonics* **4**, 011006 (2016).
- Wang, H., Zhu, J. F. & Akkin, T. Serial optical coherence scanner for large-scale brain imaging at microscopic resolution. *NeuroImage* **84**, 1007–1017 (2014).
- Odgaard, A. et al. A direct method for fast three-dimensional serial reconstruction. *J. Microsc.* **159**, 335–342 (1990).
- Chang, S. B. et al. Scalable mapping of myelin and neuron density in the human brain with micrometer resolution. *Sci. Rep.* **12**, 363 (2022).
- Bai, B. J. et al. Deep learning-enabled virtual histological staining of biological samples. *Light Sci. Appl.* **12**, 57 (2023).
- Salido, J. et al. Comparison of deep learning models for digital H&E staining from unpaired label-free multispectral microscopy images. *Computer Methods Prog. Biomed.* **235**, 107528 (2023).
- Riverson, Y. et al. PhaseStain: the digital staining of label-free quantitative phase microscopy images using deep learning. *Light Sci. Appl.* **8**, 23 (2019).
- Riverson, Y. et al. Virtual histological staining of unlabelled tissue-autofluorescence images via deep learning. *Nat. Biomed. Eng.* **3**, 466–477 (2019).
- De Haan, K. et al. Deep learning-based transformation of H&E stained tissues into special stains. *Nat. Commun.* **12**, 4884 (2021).
- Winetraub, Y. et al. Noninvasive virtual biopsy using micro-registered optical coherence tomography (OCT) in human subjects. *Sci. Adv.* **10**, eadi5794 (2024).
- Li, X. Y. et al. Unsupervised content-preserving transformation for optical microscopy. *Light Sci. Appl.* **10**, 44 (2021).
- Ozyoruk, K. B. et al. A deep-learning model for transforming the style of tissue images from cryosectioned to formalin-fixed and paraffin-embedded. *Nat. Biomed. Eng.* **6**, 1407–1419 (2022).
- Combaila, M. et al. Digitally stained confocal microscopy through deep learning. In *Proc. 2nd International Conference on Medical Imaging with Deep Learning*. (PMLR 2019).
- Kang, L. et al. Deep learning enables ultraviolet photoacoustic microscopy based histological imaging with near real-time virtual staining. *Photoacoustics* **25**, 100308 (2022).
- Zhu, J. Y. et al. Unpaired image-to-image translation using cycle-consistent adversarial networks. In *Proc. IEEE International Conference on Computer Vision*. (IEEE, 2017).
- Park, T. et al. Contrastive learning for unpaired image-to-image translation. In *Proceedings of the 16th European Conference on Computer Vision*. (Springer, 2020).
- Kong, L. K. et al. Breaking the dilemma of medical image-to-image translation. In *Proc. 35th International Conference on Neural Information Processing Systems*. (ACM, 2021).
- Qin, C. et al. Unsupervised deformable registration for multi-modal images via disentangled representations. In *Proc. 26th International Conference on Information Processing in Medical Imaging*. (Springer, 2019).
- Arar, M. et al. Unsupervised multi-modal image registration via geometry preserving image-to-image translation. In *Proc. IEEE/CVF Conference on Computer Vision and Pattern Recognition*. (IEEE, 2020).
- Ganin, Y. et al. Domain-adversarial training of neural networks. in *Domain Adaptation in Computer Vision Applications* (ed Csorika, G.) (Cham: Springer, 2017).
- Chang, S. B. et al. Multi-scale label-free human brain imaging with integrated serial sectioning polarization sensitive optical coherence tomography and two-photon microscopy. *Adv. Sci.* **10**, 2303381 (2023).
- Varadarajan, D. et al. A novel algorithm for multiplicative speckle noise reduction in ex vivo human brain OCT images. *NeuroImage* **257**, 119304 (2022).
- Palomero-Gallagher, N. & Zilles, K. Cortical layers: cyto-, myelo-, receptor- and synaptic architecture in human cortical areas. *NeuroImage* **197**, 716–741 (2019).
- Turner, R. Myelin and modeling: bootstrapping cortical microcircuits. *Front. Neural Circuits* **13**, 34 (2019).

42. Lin, D. J., Hermann, K. L. & Schmähmann, J. D. The diagnosis and natural history of multiple system atrophy, cerebellar type. *Cerebellum* **15**, 663–679 (2016).
43. Halliday, G. M. Re-evaluating the glio-centric view of multiple system atrophy by highlighting the neuronal involvement. *Brain* **138**, 2116–2119 (2015).
44. DeFelipe, J., Alonso-Nanclares, L. & Arellano, J. I. Microstructure of the neo-cortex: comparative aspects. *J. Neurocytol.* **31**, 299–316 (2002).
45. Wagstyl, K. et al. BigBrain 3D atlas of cortical layers: cortical and laminar thickness gradients diverge in sensory and motor cortices. *PLoS Biol.* **18**, e3000678 (2020).
46. Pang, C. C. C. et al. Ammon's horn 2 (CA2) of the hippocampus: a long-known region with a new potential role in neurodegeneration. *Neuroscientist* **25**, 167–180 (2019).
47. Perge, J. A. et al. Why do axons differ in caliber? *J. Neurosci.* **32**, 626–638 (2012).
48. Molini, A. B. et al. Speckle2Void: deep self-supervised SAR despeckling with blind-spot convolutional neural networks. *IEEE Trans. Geosci. Remote Sens.* **60**, 5204017 (2022).
49. Liu, R. R. et al. Deep spectral learning for label-free optical imaging oximetry with uncertainty quantification. *Light Sci. Appl.* **8**, 102 (2019).
50. Schneider, C. A., Rasband, W. S. & Eliceiri, K. W. NIH image to ImageJ: 25 years of image analysis. *Nat. Methods* **9**, 671–675 (2012).
51. Fan, J., Dawson, T. M. & Dawson, V. L. Cell death mechanisms of neurodegeneration. in *Neurodegenerative Diseases Pathology, Mechanisms, and Potential Therapeutic Targets* (eds Beart, P. et al.) (Cham: Springer, 2017).
52. Reinhard, E. et al. Color transfer between images. *IEEE Computer Graph. Appl.* **21**, 34–41 (2001).
53. Van Der Walt, S. et al. Scikit-image: image processing in Python. *PeerJ* **2**, e453 (2014).